1

2

3 **Insights from modeling and observational evaluation of a precipitating**

4 **continental cumulus event observed during the MC3E field campaign**

5

6 David B. Mechem[1], Scott E. Giangrande[2], Carly S. Wittman[1], Paloma Borque[3], Tami Toto[2], and

7 Pavlos Kollias[3]

8

9 1. University of Kansas, Lawrence, KS, USA

10 2. Brookhaven National Laboratory, Upton, NY, USA

11 3. McGill University, Montreal, QC, Canada

12

16

17

18

19 Corresponding author: David B. Mechem, Atmospheric Science Program, University of Kansas,

20 1475 Jayhawk Blvd., 213 Lindley, Lawrence, KS 66045

21 Email: dmechem@ku.edu

22 Phone: 785-864-5707

23

24

Abstract

A case of shallow cumulus and precipitating cumulus congestus sampled at the Atmospheric Radiation Measurement (ARM) Program Southern Great Plains (SGP) supersite is analyzed using a multi-sensor observational approach and numerical simulation. Observations from a new radar suite surrounding the facility are used to characterize the evolving statistical behavior of the precipitating cloud system. This is accomplished using distributions of different measures of cloud geometry and precipitation properties. Large-eddy simulation (LES) with size-resolved (bin) microphysics is employed to determine the forcings most important in producing the salient aspects of the cloud system captured in the radar observations. Our emphasis is on assessing the importance of time-varying vs. steady-state large-scale forcing on the model's ability to reproduce the evolutionary behavior of the cloud system. Additional consideration is given to how the characteristic spatial scale and homogeneity of the forcing imposed on the simulation influences the evolution of cloud system properties. Results indicate that several new scanning radar estimates such as distributions of cloud top are useful to differentiate the value of time-varying (or at least temporally well-matched) forcing on LES solution fidelity.

41

1. Introduction

Much of the uncertainty in climate model projections stems from our limited understanding of cloud and precipitation processes, and the parameterization of these processes in global climate models (GCMs). While representing deep convective clouds in GCMs remains an ongoing problem (Stevens and Bony 2013), the treatment of shallow clouds such as stratocumulus and trade cumulus also plays a crucial role in climate system modeling. Because of their high albedo, broad areal coverage, and high radiating temperature (i.e., low, warm cloud tops), stratocumulus produce a climatologically important cooling effect on the climate system (Hartmann et al. 1992; Klein and Hartmann 1993). The moistening and cooling from shallow cumulus balance the warming and drying from large-scale subsidence. Turbulent fluxes from shallow cumulus clouds thus help determine the steady-state depth and thermodynamic properties of the trade-wind boundary layer (Riehl et al. 1951; Stevens 2007; Rauber et al. 2007) and perhaps precondition the lower atmosphere for deeper convective events (e.g., Johnson et al. 1999; Waite and Khouider 2010).

Representing shallow clouds and their transitions in GCMs is a major challenge (Bony and Dufresne 2005; Wyant et al. 2007; Medeiros et al. 2008). Typically, results from cloud-resolving models (CRMs) or large-eddy simulation (LES) models serve as benchmarks for developing and tuning single-column models (SCMs). These SCMs in turn often form the basis of parameterizations in GCMs. Thus, LES is positioned as a key tool for investigating cloud-system processes (e.g., aerosol indirect effects). For example, LES intercomparisons under the GCSS/GASS (GEWEX [Global Energy and Water Exchanges Project] Cloud Systems Study/Global

64   Atmospheric System Studies) framework have been fruitful (e.g., Moeng et al. 1996; Bretherton

65   et al. 1999; Stevens et al. 2001; Brown et al. 2002; Seibesma et al. 2003; Stevens et al. 2005;

66   Ackerman et al. 2009; van Zanten et al. 2011), and simulations from these intercomparisons

67   have served as a benchmark for SCMs and associated parameterization development (e.g.,

68   Lenderink et al. 2004; Zhu et al. 2005; Wyant et al. 2007). However, this GCSS/GASS paradigm

69   investigates model pathologies largely using intercomparisons of simulations, placing less

70   emphasis on evaluating LES solutions against observational constraints. One noteworthy

71   exception to this approach was the DYCOMS–II (Dynamics and Chemistry of Marine

72   Stratocumulus; Stevens et al. 2003) model intercomparison (Stevens et al. 2005), in which

73   model representations of entrainment rate were compared to innovative new aircraft

74   observations of cloud-top entrainment (Faloona et al. 2005).

75   One explanation for a de-emphasis on observations is that shallow clouds are difficult to

76   reliably sample, and our existing observational capabilities are often incompatible with high-

77   resolution LES models. Although shallow cloud observations are collected over a handful of

78   ground-based supersites (Stokes and Schwartz 1994; Ackerman and Stokes 2003; Illingworth et

79   al. 2007; Mather and Voyles 2013), comprehensively sampling elusive targets such as shallow

80   cumulus requires merging a wide array of active and passive cloud sensors, together with

81   support from aircraft (e.g., Vogelmann et al. 2012). Newer approaches employing Doppler radar

82   spectra can give dynamical and microphysical insights into shallow clouds, but until recently

83   these techniques have been computationally prohibitive (e.g., Kollias et al. 2011; Luke and

84   Kollias 2013). Adding to these challenges, the majority of high-resolution datasets has been

85   restricted to single column, or 'pencil beam' measurements from millimeter-wavelength radars

86 that must represent transient cloud and precipitation behaviors across scales from typical

87 LES/CRM domain sizes (~4–40 km^2) to GCM (grid box) scales (~100 km^2).

88   This study documents our preliminary effort toward a more natural coupling of LES

89 modeling and cloud observing capabilities for one particular ground-based supersite. This site is

90 the Oklahoma Southern Great Plains (SGP) location operated by the Department of Energy

91 (DOE) Atmospheric Radiation Measurement (ARM) program centered at Lamont, Oklahoma.

92 The site recently complemented its single-column measurements with new scanning radar that

93 may better suit the sampling of LES-scale domains. We consider an application of LES with size-

94 resolved (bin) microphysics as one avenue for capitalizing on the fine details sampled by these

95 new radar facilities. Observations from radar systems should compare favorably with bin

96 microphysical models that are better capable of reproducing radar measurements from drop-

97 size distributions and high-resolution turbulent flow fields (e.g., Kollias et al. 2011). An

98 overarching objective is to determine whether scanning radars provide useful model

99 constraints for documenting the time-evolving structure of clouds, precipitation, and associated

100 processes around this ARM site (Mather and Voyles, 2013; Kollias et al., 2014). An additional

101 emphasis is to evaluate the sensitivity of cloud and precipitation properties to differences in the

102 spatial scale and temporal details of the large-scale forcing.

103   We investigate the sensitivity of LES solutions to changes in spatial and temporal large-

104 scale forcing for a challenging shallow cumulus and congestus event. We emphasize the

105 transient nature of the forcing (i.e., time-varying vs. steady-state) and its importance on

106 simulation outcome. This is accomplished by assessing the extent to which ensemble members

107 reproduce salient observed macrophysical cloud field properties over the ARM facility (e.g., Xu

108   et al. 2002; 2005; Xie et al. 2005; Mechem et al. 2010). The counterargument, that a model

109   must first reproduce microphysical processes in order to faithfully represent macroscale

110   properties, is also valid. Although evaluating LES performance against macroscale cloud

111   properties is often the easier task and the approach this study adopts, improvements to LES

112   macroscale and microscale cloud property representations are intrinsically iterative.

113   The paper is outlined as follows. A synoptic overview of the event and the associated

114   model forcing considerations is presented in Section 2. The event is analyzed using a multi-

115   sensor observational approach and numerical simulation as described in Sections 3 and 4. A

116   discussion on the sensitivity of LES macroscale properties as evaluated against ARM

117   observations is provided in Section 5. Key findings are summarized in Section 6.

118

119

2. The 25 May 2011 Congestus Event: Synoptic Overview and Cloud Forcing

This study focuses on a strongly forced case of shallow cumulus transitioning to precipitating cumulus congestus. The clouds were observed on 25 May 2011 during the DOE ARM and National Aeronautics and Space Administration (NASA) Global Precipitation Measurement (GPM) mission campaign, the Midlatitude Continental Convective Clouds Experiment (MC3E; Jensen et al. 2010). Clouds developed following a frontal passage and a period of deeper convection connected with a mature low-pressure system over central Kansas (Fig. 1). Shallow clouds formed over the SGP site by 1500 UTC (0900 CST). The clouds surrounding the SGP facility gradually transitioned to scattered cumulus congestus by midday (1800 UTC; 1200 CST), and isolated, comingled, precipitating congestus thereafter. Winds at cloud level naturally shifted from southwest to northwest as the low-pressure system progressed eastward by the afternoon (late UTC) hours.

An idealized perspective on the evolution of the 25 May 2011 synoptic conditions can be constructed from MC3E measurements using the variational analysis method of Zhang and Lin (1997; as also in Xie et al. 2014). These analysis fields serve as the forcing dataset for the simulations presented in this study (e.g., Fig. 2, Table 1). In addition to these multi-scale forcing datasets, the MC3E campaign launched radiosondes at 3-hour intervals from 6 locations within a 150-km radius of the SGP Lamont central facility (Jensen et al. 2015; locations highlighted in Fig. 1). Figure 2 shows time-height representations of several fields from the variational analysis product. This figure includes potential temperature and moisture advection, as well as vertical motion, at two characteristic spatial scales (75 km and 150 km). These characteristic

142   forcing domains are centered on the SGP central facility in Lamont, Oklahoma (Fig. 1).

143   Using the forcing fields in Fig. 2 as a guide, the gradual deepening of the clouds from

144   shallow cumulus to congestus can be attributed to several factors. The northern Oklahoma

145   region experienced positive low-level moisture advection (from the surface up to ~800 mb)

146   throughout the event. This moist advection included moisture advected from the Gulf of

147   Mexico wrapping around the mature low-pressure system. Throughout the day, a deep layer of

148   cold advection (from the surface up to a level of 650–500 mb aloft, depending upon the time

149   and analysis scale) brought the layer closer to saturation and likely promoted cloud

150   development. Upward vertical motion overlaid low-level subsidence (or very weak vertical

151   motion), although the relative strength of these features depended greatly on the scale of the

152   forcing.

153

154

3. ARM SGP Site Observations and Cloud Macroscale Properties

The cloud macroscale properties selected for this 25 May 2011 LES sensitivity study rely on the radar observations now routine for the ARM SGP. For simplicity, we limit this discussion to four observational quantities when evaluating the LES ensemble solutions. Our first consideration when selecting these products is to target cloud properties simple to estimate from radar, focusing in particular on fields less susceptible to known radar challenges such as miscalibration or attenuation in cloud/rain (e.g., Ryzhkov et al. 2005; Kollias et al. 2014). Our efforts emphasize macroscale cloud properties that follow naturally from LES model outputs without the need for advanced forward-radar modeling or computations.

Historically, the ARM radar datastream most referenced for the evaluation of LES cloud simulations is the ARSCL product (Active Remote Sensing of CLouds; Clothiaux et al. 2000; Kollias et al. 2005). This radar product merges observations from the vertically-pointing 35-GHz Ka-band radar (KAZR), collocated laser ceilometer, micropulse lidar, and microwave radiometer to identify cloud boundaries in the vertical profile. New scanning radar capabilities complement those single column cloud insights in several ways. Precipitating cell properties are now available to within 150 km of the SGP Lamont site using the surveillance 5.4-GHz ARM C-band Scanning ARM Polarimetric weather Radar (C-SAPR) and the nearby KVNX WSR-88D (e.g., Giangrande et al. 2014). MC3E also unveiled the first generation of ARM dual-frequency 35/94-GHz (Ka/W-band) Scanning ARM Cloud Radars (SACR, e.g., Kollias et al. 2014). During MC3E, the SACR system sampled cloud elements using 2D slices (range-height; RHI) to quickly track cloud features in time and evaluate their geometric properties (e.g., Borque et al. 2014). The four

177   estimates of cloud-system properties as obtained from these facilities are briefly discussed

178   below.

179

180   *a. Cloud Fraction (CF)*

181   Cloud Fraction (CF) is widely considered for model performance evaluation (e.g.,

182   Bedacht et al. 2007; Wilkinson et al. 2008; Walsh et al. 2009). Interpreting observational CF

183   estimates that best align with model CF definitions is nontrivial, since current observations are

184   unable to unambiguously reconstruct an instantaneous 3D cloud field (e.g., Wiscombe 2005;

185   Wu et al. 2014). This study considers five observational definitions for CF that range from 1D,

186   column-based radar approximations to satellite-based horizontal integrations over spatial

187   footprints comparable to LES domain sizes. Our analysis includes the following estimates of CF:

188   ● The 2D VISST (Visible Infrared Solar-Infrared Split Window Technique) height-

189   integrated GOES geostationary satellite estimate. This technique estimates the

190   'cloudy pixel' area relative to the 0.5 x 0.5 degree latitude-longitude grid box that

191   overlaps with the ARM SGP (Minnis et al. 2011).

192   ● The CF estimates from 2D hemispheric projections obtained using an ARM Total Sky

193   Imager (TSI) camera (Kassianov et al. 2005; Long et al. 2006).

194   ● An estimate using shortwave radiation measurements from the ARM Solar Infrared

195   Radiation Station (SIRS) data (Xie and Liu 2013).

196   ● From the ARM radars, the standard ARM vertically pointing ARSCL definition that

197   defines CF as the fraction of an hour that the radar/lidar column designates cloud

198   echo overhead.

199   ● A new CF approach, developed from the 25 May 2011 MC3E radar dataset (Borque et

200   al. 2014) that uses SACR "along-wind" RHI modes. This CF estimate is defined by

201   projecting the horizontal area covered by cloud elements sampled along the 40-km

202   RHI slice. Since the scanning orientation follows the prevailing wind, these estimates

203   assume cloud fraction is homogeneous over the domain in the cross-wind direction.

204

205 *b. Cloud Top Distributions*

206   Several studies of cloud populations in the tropical environment have documented

207 cloud tops that coincide with the trade-wind inversion or the weakly stable layer often present

208 at the melting level (e.g., Johnson 1999; Jensen and Del Genio 2006; Mechem and Oberthaler

209 2013). Spaceborne systems can help document cloud top distributions and evolution, especially

210 when coupled with temperature profile information (e.g., Mace et al. 2009; Luo et al. 2010).

211 However, spaceborne and surface weather radar methods are most reliable for documenting

212 the cloud life cycle of cumulus congestus and deep convection. For shallow cumulus and

213 congestus properties, the high sensitivity and rapid scanning ability of the SACR promoted

214 sampling of the time-evolving distribution of cloud tops during the 25 May 2011 event.

215   Figure 3a (adapted from Borque et al. 2014) documents transitions between periods of

216 solely shallow cumulus, periods of commingled shallow and congestus clouds, and periods of

217 primarily congestus clouds. The modes are reflected in the cloud-top height distribution, where

218 we see a narrow upper-level distribution mode between about 4-5 km, representing primarily

219 cumulus congestus periods, and a broader distribution representing shallow cumulus and

220 commingled times. Please note that although the upper portions of the congestus clouds are

221   colder than their tropical counterparts (Mechem and Oberthaler 2013) and may reach

222   temperatures down to -10°C, for our simulation purposes we assume they are largely governed

223   by warm-rain microphysical processes (an assumption we address in Sec. 4c). Precipitation

224   onset and the subsequent generation of cold pools, in this case, are reflected in the cloud top

225   distribution. We confirm the former by consulting the corresponding rainfall rate time series

226   based on nearby ARM systems (Fig.   3b). These rainfall rate traces in Fig.   3b include

227   measurements from the surface disdrometer in close proximity to the SACR, and an averaged C-

228   SAPR estimate collected along the SACR scanning path. The presence of precipitating cumulus is

229   confirmed by considering the enhancements in higher cloud top height counts at the expense

230   of lower-topped clouds. These time-height distributions complement traditional CF estimates

231   less capable of differentiating multi-layer or commingled cloud types. However, these

232   observations from the 25 May 2011 SACR dataset are somewhat noisy and reflect some limits

233   of the current ARM single radar sampling strategies (only approximately 2.5 hours of data from

234   the date under investigation). Thus, a combination of multi-platform observations (e.g., ARSCL,

235   TSI, SIRS, GOES), for cross-validation, provides additional support for interpretations of the

236   limited SACR observations.

237   Despite the single-column limitations mentioned above, the KAZR–ARSCL product

238   provides an additional perspective on cloud system behavior over the period (Fig. 4). From

239   1500–1700 UTC, the KAZR does not capture the isolated shallow cumulus visible in the TSI (not

240   shown). However, starting at 1700 UTC, the radar does sample a cloud layer that deepens and

241   increases in cloud fraction over the next 2 hours. Designated cloud top heights then undulate

242   by ~1 km in height from 1900–2100 UTC. KAZR-ARSCL cloud tops and hydrometeor fraction

243 (Figs. 4a and b) hint at the bimodal (multi-layer) cloud structure suggested by the SACR

244 statistics in Fig. 3. Some differences in cloud statistics in Figs. 3. and 4 during overlapping

245 sequences may be partially attributable to fundamental differences in scanning strategies and

246 capture volumes between the Ka–SACR (RHI) and the KAZR (profiling).

247

248 *c. Areal Precipitation Fraction and Totals*

249 A common weather radar application is to document surface rainfall accumulation and

250 precipitating cell properties (e.g., Doviak and Zrnic 1993). For climate model applications, this

251 may include properties such as domain-mean precipitation rate, accumulation, and time-

252 varying behaviors. Fractional area of a representative domain covered by precipitation is one

253 such property and is analogous to spatially averaged CF estimates. For this study, precipitation

254 area fraction can be estimated from the C-SAPR dataset by calculating the area covered by

255 near-surface radar reflectivity factor Z exceeding a minimum threshold. The selection of a 30-

256 dBz threshold is based on previous warm-season precipitation studies in the vicinity of the ARM

257 SGP site (e.g., Giangrande et al. 2012; Giangrande et al. 2014). To allow for a range of radar

258 measurement uncertainty in light rain conditions, this study considers a spread of area fraction

259 corresponding to a less-restrictive 25-dBz threshold and a more-restrictive 30-dBz threshold.

260 For domain-mean precipitation accumulations, the simulations are forced with

261 horizontally homogeneous profiles representative of 75-km and 150-km diameter circles

262 centered on SGP Lamont. Radar rainfall products are available at high resolution and may be

263 resampled to those domains. The variational approach that generated the forcing datasets was

264 constrained using surface precipitation estimates from the Arkansas River Basin Forecast Center

13

265 (ARBFC) 4x4 km hourly WSR-88D radar–surface gauge hybrid rainfall product (e.g., Young et al.

266 2000). The forcing from the variational analysis is therefore constrained by these mean rainfall

267 estimate products, which should then be reflected in model behavior. However, the influence

268 of this precipitation constraint on the forcing (mediated through diabatic heating and drying of

269 the column) should be weak based on the small value of domain-mean precipitation relative to

270 cases involving substantial precipitation (e.g., Xie et al. 2014). We compare LES domain-mean

271 rainfall properties to those from an unattenuated standard gauge-adjusted WSR-88D radar

272 rainfall product, the National Mosaic and Multi-Sensor Quantitative Precipitation Estimation

273 (NMQ) product (e.g., Zhang et al. 2005). For this event, the accumulations were nearly identical

274 to those of the ingested ARBFC products, providing additional confidence in the quality of these

275 areal precipitation estimates.

276

277 **4. Large-eddy Simulation**

278

279 *a. Model Configuration and Microphysics*

280   All simulations here use the System for Atmospheric Modeling — Explicit Microphysics

281 (SAMEX). SAMEX employs the anelastic dynamical core from the System for Atmospheric

282 Modeling (SAM; Khairoutdinov and Randall 2003) and has been successfully used in a number

283 of numerical modeling efforts (van Zanten et al. 2011; Kogan et al. 2012; Mechem et al. 2012).

284 In this study, we configure SAMEX in a manner roughly similar to that of the RICO (Rain in

285 Cumulus over the Ocean; Rauber et al. 2007) trade cumulus intercomparison (van Zanten et al.

286 2011). For these simulations, SAMEX employs a horizontal grid spacing of 100 m and a constant

287 vertical spacing of 50 m. Previous studies demonstrate the importance of using fine vertical grid

288 spacing for representing cumulus congestus (Khairoutdinov et al. 2009; Mechem and

289 Oberthaler 2013). The number of grid points is 384x384x160 to yield a domain size of

290 38.3x38.3x8 km^3, a volume that captures the cloud system mesoscale variability reasonably

291 well. This experimental setup is employed as a starting point for the simulation suite. A

292 simulation quadrupling the horizontal domain area (768x768x160 points) exhibits similar

293 behavior to our baseline grid configuration for the majority of the simulation period.

294   SAMEX employs an explicit representation of microphysical processes (Kogan 1991) that

295 includes size-resolving representations of droplets and cloud condensation nuclei (CCN). The

296 model predicts distribution functions for CCN and liquid droplets, and solves the stochastic

297 collection equation for the droplet spectra at all model grid points. As mentioned in Sec. 3b, our

298 simulations assume warm-rain microphysical process dominate. The SAMEX configuration for

15

299   our simulations uses 19 CCN bins and 34 mass-doubling droplet bins that range in size from 1

300   μm to 2.05 mm in radius. The number of bins is the same as used in the RICO trade cumulus

301   (van Zanten et al. 2011) and VOCALS southeast Pacific stratocumulus (Mechem et al. 2012)

302   simulations. We assume an initial CCN concentration of 425 cm^{-3} (at a supersaturation S =

303   0.47%) as directly measured from the ARM CCN counter at SGP, distributed in a lognormal

304   spectrum with geometric mean radius of 0.03 μm and standard deviation of 1.28 μm. This

305   spectral shape is similar to that used in previous RICO and VOCALS simulations. In our

306   experience, simulation results are more sensitive to differences in total aerosol concentration

307   than they are to modest differences in aerosol distribution shape. We more rigorously address

308   this assumption in Sec. 4c. Our simulations neglect shortwave and longwave heating, which we

309   justify given that the magnitude of the large-scale forcing appears to be the most dominant

310   factor governing cloud-system evolution. Short-duration simulations including longwave and

311   shortwave radiative forcing exhibit only minor differences relative to the simulations without

312   radiative forcing.

313

314   *b. Model Initial Conditions and Forcing*

315   All simulations use the semi-diagnostic modeling framework in which the model

316   responds to observationally-constrained forcing fields of temperature and moisture (e.g., Wu et

317   al. 1998; Xu et al. 2002, 2005; Xie et al. 2005; Zeng et al. 2009; Mechem and Oberthaler 2013).

318   Figure 2 shows the large-scale advective tendencies, vertical motion, and surface heat and

319   moisture fluxes imposed as forcing for the simulations. Although we refer to these quantities as

320   "large-scale," they are characterized by 75- and 150-km analysis scales shown in Fig. 1 and

321 therefore include some degree of mesoscale variability, in addition to contributions from the

322 synoptic and planetary scales. Table 1 summarizes the forcing configurations for the seven

323 simulations in our ensemble, largely differing in the way the forcing fields are imposed (e.g.,

324 time-varying vs. steady-state). The forcing terms in Table 1 are an attempt to distill each forcing

325 profile (which vary in the vertical and, depending on the simulation, in time) shown Fig. 2 into a

326 single "bulk" number for each forcing quantity.

327 The control simulation (1200v_75) assumes horizontally homogeneous initial profiles of

328 temperature, moisture, and momentum from the 75-km-scale variational analysis at 1200 UTC.

329 Over the course of the 9-hour simulation, profiles of time-varying horizontal advection and

330 vertical velocity are imposed on the domain (see the shaded boxes covering the 1200–2100

331 UTC period on the 75-km-scale panels in Fig. 2). We consider the first three hours of the

332 simulation as a model spin-up period, until the integrated turbulent kinetic energy (TKE, not

333 shown) reaches a near-steady state. Thus, the discussion of simulation results Section 5

334 includes only the final 6 simulation hours. Over the simulation period from 1200–2100 UTC, all

335 vertical levels below 600 mb exhibit negative potential temperature (cold) advection (Fig. 2a

336 and b). Since the advection over this layer is largely constant with height, we surmise that the

337 effect on static stability over the cloud layer is minimal; in other words, the cold advection has

338 neither a stabilizing nor a destabilizing influence. However, all else being equal, stronger cold

339 advection will promote saturation (and hence cloud development) more quickly. Moisture

340 advection (Figs. 2c and d) is significantly positive below 800 mb, which should enhance

341 instability over the course of the simulation. At 1200 UTC, subsidence dominates the large-scale

342 vertical motion field below 600 mb (particularly at the 75-km scale; Fig. 2e), and the magnitude

17

343   of subsidence decreases over the course of the simulation. Thus, the stabilizing effect of

344   subsidence on the mean stratification should decrease with time.

345   The potential temperature and moisture advection at the 150-km scale (1200v_150

346   simulation) is qualitatively similar to those terms at the 75-km scale, although the moistening is

347   shallower and overlaid by a layer of weak drying. The large-scale vertical velocity fields,

348   however, differspu substantially. The layer of subsidence below 650 mb that is slowly

349   weakening with time at the 75-km scale is replaced at the 150-km scale with an elevated layer

350   of ascent. Note that the values of vertical velocity over the course of the simulations are rather

351   weak relative to the strong ascent associated with the frontal passage that occurred between

352   0200 and 0300 UTC. Thus, the effect of the large-scale vertical velocity on simulation outcomes

353   is not obvious *a priori*.

354   All other simulations assume the forcing is constant in time. For example, in the

355   1800s_75 simulation, initial conditions are taken from 1800 UTC, and the same 1800 UTC

356   forcing is imposed over the entire 9-hour simulation. These steady-state, fixed-in-time

357   simulations serve to evaluate the importance of the evolutionary nature of the forcing.

358   Although we refer to the simulations as "steady-state," the simulations reach a condition

359   resembling steady-state behavior only during the final hours of the simulations. Moreover,

360   imposing constant forcings over the course of a simulation may have unintended

361   consequences. One simulation (1200s_75, not shown) develops a spurious, unphysical layer of

362   mid-level cloud that results from constantly imposing moistening and cooling over the entire

363   course of the simulation.

364

365   *c. Additional Model Considerations*

366   Our simulations employ CCN concentration as measured at the surface. We assume that

367   this measured concentration is representative of CCN at cloud base, which in the well-mixed

368   boundary layer present in this case is a reasonable assumption. We argue above in Sec. 4a that

369   simulated cloud properties are more sensitive to differences in total aerosol concentration than

370   they are to modest differences in aerosol distribution shape. Thus, for this study we use the

371   spectral shape we have employed previously in simulations of RICO and VOCALS cases. We

372   evaluate this conjecture by conducting a variation of the 1200v_75 simulation where the total

373   CCN concentration is maintained, but the breadth (standard deviation) of the CCN spectrum is

374   increased by 50%. Differences between the two simulations (not shown) are miniscule,

375   particularly for integrated quantities such as boundary layer depth and total precipitation. This

376   finding is unsurprising given the strong congestus updrafts contain large values of

377   supersaturation likely to activate all but the smallest of hygroscopic aerosol. Exploring

378   differences in CCN concentration would be a natural choice for additional sensitivity simulations

379   but is beyond the scope of the present study.

380   Because the cloud tops of some cumulus congestus within the domain may lie above the

381    $0°C$ line, ice may be present. Congestus clouds are typically thought to be dominated by warm-

382   rain, collision–coalescence processes (Lasher-Trapp et al. 2001; Mechem and Oberthaler 2013),

383   though ice-phase processes may play a role in deeper congestus (Johnson et al. 1999). The bin-

384   microphysics parameterization represents the evolution of only the liquid part of the

385   condensate. However, in an attempt to estimate the importance of ice-phase processes for this

386   event, we conducted additional bulk microphysical simulations of the 1200v_75 and 1500s_75

387 cases. These simulations used the 2-moment Morrison et al. parameterization (Morrison et al.

388 2005), with and without ice-phase processes. For these tests, ice-phase processes had only a

389 modest effect on the simulation results, increasing accumulated precipitation by ~8% and ~6%

390 in the 1200v_75 and 1500s_75 simulations, respectively. Furthermore, radar observations for

391 this event also suggest the reasonableness of the warm-rain assumption. In particular, the

392 observed cloud behaviors in Borque et al. (2014) demonstrate the lack of a prominent radar

393 bright band / ice-media melting signature. When a bright band is visible on radar, very little

394 cloud depth extends above it.

395

396

397

398

5. Ensemble Performance for the 25 May 2011 Event

A snapshot of the model-generated radar reflectivity field for the 1200v_75 control simulation at 1500 UTC shows an array of shallow cumulus, deeper cumulus clouds, and strongly precipitating cumulus congestus (Fig. 5). Mean LES ensemble member performance metrics and time series of LES ensemble and observational results for the 25 May 2011 event are presented in Tables 2-3 and Figs. 6-8, respectively. The tables document LES results according to two periods of 3-hour averages of the cloud field properties that are representative of "early event" periods (3 h to 6 h simulation time; 1500–1800 UTC; Table 2) and "late event" periods (6 h to 9 h simulation time; 1800–2100 UTC; Table 3). These periods were determined according to the observed precipitation onset time (~6h simulation time; 1800 UTC). For the time-varying forcing configurations (labeled 'v' in Table 1), early and late event breakdowns should roughly correspond to the intervals of shallow cumulus (early) and subsequent precipitating congestus (late) conditions. For the steady-state runs (labeled 's' in Table 1), early period averages reflect LES solutions from the 3-hour period (3h to 6h) that immediately followed the 3-hour model spin-up. Late event results highlight the cloud properties from the final 3-hour period (6h to 9h), at a time when the observations and all featured simulations indicate precipitating clouds.

a. Cloud Fraction

Cloud fraction observations and simulation results are summarized in Fig. 6. The different observational CF estimates are consistent (~70–90% CF) over the later period, when

421   congestus were present. A significant spread in estimates was observed during the shallow

422   cumulus period prior to precipitation onset (~10–90% CF). The VISST satellite-based product

423   ("GOES low+med" in Fig. 6) estimated the largest CF, with a sizeable component of this CF value

424   attributed to mid-to-upper level clouds (~8 km altitude) wrapping into the northern sections of

425   the domain. The CF values estimated by narrower field-of-view ARM sensors (TSI, SIRS, and

426   ARSCL) were consistent with campaign visual reports of scattered low cumulus transitioning to

427   a more overcast cloud field populated by congestus (e.g., Figs. 4 and 6). The SACR CF estimate

428   adopted by this study was unavailable prior to 1830 UTC, and when available reported the

429   lowest CF values when congestus were present (~60%). TSI and satellite images indicate that

430   the discrepancy is partially the consequence of directional sampling limitations. Specifically, the

431   SACR scanning prioritized a direction along the prevailing northwesterly wind such that half of

432   the radar RHI was performed toward the southeast, the region least favorable for cloud

433   development.

434   For the early cloud period, all LES solutions ostensibly overestimated CF (Fig. 6, gray and

435   black shading and control lines; Table 2) compared to the median observational estimate of

436   0.49 calculated from 1500 to 1800 UTC. Comparisons with CF observations suggest the most

437   credible shallow cumulus representation was obtained when applying time-varying forcing

438   conditions initiated at 1200 UTC (1200v_75, 1200v_150). These two forcing configurations

439   include the constraints that we expected would best capture the time-evolution of cloud

440   system properties for this challenging transition event. A reversal in model–observation CF

441   characteristics was observed following precipitation onset, with the ensemble members

442   underpredicting the CF associated with the congestus mode as compared to the observational

443 consensus (e.g., Fig. 6, Table 3). One noteworthy exception was the 2100s_75 simulation that

444 predicted extensive cloud coverage associated with low-topped cumulus (cloud top heights of

445 ~3 km, Table 3). The time-evolving forcing configurations, and the steady-state configurations

446 corresponding to the times when congestus were present, typically resulted in higher CF values

447 and better agreement with CF observations during the late-event period. Beyond 9 hours,

448 several of the steady-state runs trend toward a domain-limited behavior of a few prominent

449 cloudy cells.

450   The usefulness of CF comparisons beyond this basic qualitative agreement is not clear.

451 Cloud fraction is an important quantity via its influence on the radiation budget, and therefore

452 it constitutes a bulk measure of the cloud system that models should strive to simulate.

453 However, as a tool for diagnosing model pathologies (i.e., the root cause of model–observation

454 mismatch and how to fix it), CF is inadequate. Furthermore, the SAMEX modeling framework is

455 highly idealized and assumes horizontally homogeneous initial conditions and forcing. For this

456 study, the prevailing forcing of positive moisture advection and negative potential temperature

457 advection (e.g., Table 1) is conducive to simulating the observed transition from shallow clouds

458 to a field that includes both shallow cumulus and congestus. The homogeneity of forcing,

459 however, dictates that clouds initiate with an equal likelihood everywhere within our LES

460 domain. In other words, cloud behavior is statistically homogeneous across the model domain,

461 in contrast to the highly variable spatial structure visible in Fig. 1. The SACR observations, on

462 the other hand, indicate a cloud population that is not statistically homogeneous. For this

463 reason, CF metrics between the statistically homogeneous simulations and the horizontally

464 heterogeneous observational cloud field may differ substantially.

465   During the later period when congestus are present, LES CF values are closer to the

466   observations (median value of 0.85 from 1800 to 2100 UTC). Based on similar arguments as

467   above, this agreement may be fortuitous. We note that LES solutions progress towards stronger

468   isolated congestus reminiscent of the deep precipitating congestus clouds sampled by the C-

469   SAPR. However, the LES behavior of a simple evolution from shallow cumulus to isolated

470   deeper congestus conflicts with the complexity found in the ARM CF observations that favor

471   the coexistence of a spectrum of cloud depths; these include the deep, strongly precipitating

472   congestus, and also weaker congestus elements and commingled shallow cumulus clouds.

473   Although we cannot address this discrepancy with certainty, we speculate that the differences

474   may arise from the highly idealized nature of the forcing, particularly in two respects: First,

475   since the piecewise continuous forcing is applied at three-hour intervals, we should not

476   necessarily expect the model to reproduce fine-scale cloud behavior in time. Second, the

477   forcing profiles and doubly periodic boundary conditions impose an assumption of statistical

478   homogeneity across the simulation domain, whereas the observed transient cloud system

479   exhibits substantial horizontal variability over the same scale.

480

481

482   *b. Cloud Top Distributions*

483   LES cloud-field median and 90th percentile tops for all simulations (Tables 2, 3) were

484   consistent with SACR and ARSCL observations of the tail end of distributions of shallow cumulus

485   transitioning to later congestus. The 90th percentile values typically range from top heights less

486   than 4 km early, to heights of 5.5–6 km at later stages. In this simple manner, the two-

487   dimensional SACR observations are immediately useful for providing a more realistic range for

488   cloud top and bottom heights (e.g., Fig. 3) as compared to traditional column-based radar

489   observations (e.g., Fig. 4). Further, SACR time series depictions of the cloud top distributions

490   (Fig. 3) provide additional support for scrutinizing the evolution of LES cloud fields. For this

491   event, the results emphasize the benefits of forcing that closely mimics observations (either

492   time-varying or well-matched to the observational period of interest). For example, the most

493   accurate depiction of the cloud top distribution is found when using the time-varying forcing

494   (1200v_75, 1200v_150). These simulations properly capture the bimodal cloud top features in

495   the observations (Fig. 3, 4) and suitably delay the initiation of significant congestus to better

496   match with precipitation onset timing (see the precipitation onset lines in Fig. 7 and the

497   evolution of precipitating echo area in Fig. 8). The 1500 UTC and 1800 UTC steady-state forcings

498   also developed bimodal cloud top behaviors (Fig. 7) characteristic of those observation times.

499   The reason for the bimodal cloud behavior is not clear, but preliminary analysis suggests that

500   variations in low-level stability may lead to differences in cloud depth, precipitation initiation,

501   and subsequent cloud-system behavior. The early steady-state forcing conditions (1200 UTC)

502   preclude rapid development of precipitating congestus, whereas using later steady-state

503   forcing (2100 UTC) results in a cloud population with characteristic tops inconsistent with

504   observations (e.g., Fig. 7).   Although SACR insights are beneficial, the limits of the SACR

505   scanning strategy employed for the 25 May 2011 case suggests that additional radars and

506   scanning modes are required to fully characterize three-dimensional distributions of cloud

507   properties.

508

c. Precipitation Behavior

509

510   In following the progression towards deeper congestus, LES ensemble members

511   overestimate the areal coverage and amount of precipitation (Fig. 8, Table 3). The temporal

512   variability of precipitation fraction (area fraction ~0.01–0.1) and the mean precipitation over

513   the domain from the LES lacks the slower, gradual build-up of these precipitation quantities as

514   viewed by the C-SAPR. Nevertheless, new radar insights still suggest some benefit to well-

515   matched forcing conditions. For example, early (3h–6h) sequences from the 1800 UTC runs

516   (Table 2) predicted reasonable 3-hour average or accumulated behaviors for radar cloud tops

517   (~4.5-5.0 km), CF (~0.7-0.9), precipitation totals (~0.5-0.6mm), and areal fraction (~0.05-0.08),

518   as compared to the observations between 1800–2100 UTC. Of all the simulations, the 1200 UTC

519   time-varying runs performed best at capturing the extended event and cloud transition, as

520   gauged by the time-evolving areal coverage and rainfall totals. In particular, the later

521   precipitation onset in these simulations better matched the observed precipitation onset.

522   Precipitation totals for the two time-varying simulations were in the middle of the ensemble

523   (~1.2 mm of total precipitation), and the modest areal fraction (< 0.01 early, 0.05 late)

524   compared favorably to observations.

525   The authors include forcings at multiple scales (75 km, 150 km) in Table 1 to highlight

526   the challenges when attempting to interpret the impact of forcing scale on precipitation

527   behavior. Total precipitation rates for the 1800s_75 and 1800s_150 simulations are similar

528   (1.28 vs. 1.46 mm d^{-1}), yet the temperature advection, moisture advection, and vertical motion

529   differ substantially (Table 1). These results suggest a balance whereby the weaker temperature

530   and moisture advection in the 150-km simulation are compensated for by enhanced upward

531   vertical motion. We note that strong large-scale ascent was not typical of the model

532   configurations that represented precipitation onset timing favorably relative to the

533   observations. For example, the run with the highest precipitation (1500s_75) featured the least

534   favorable large-scale vertical motion, but the highest moisture advection. Ultimately, the ability

535   to predict the evolution of cloud and precipitation properties from these simple bulk measures

536   of forcing in Table 1 is limited. This simplistic interpretation of the forcing also fails to diagnose

537   unexpected behavior in select runs, such as the 2100s_75 simulation that initiates densely

538   packed precipitating cumulus that bear no resemblance to the cloud radar observations. As we

539   mention above in Sec. 5b, results suggest that differences in low-level stability may be

540   important in controlling the initial precipitation onset, a notion we will explore in further study

541   of our simulation ensemble.

542   For radar-based observations from the C-SAPR and WSR-88Ds, the choice of spatial scale

543   had little impact on the precipitation properties considered. Although the choice of scale was

544   influential to the performance of several of the LES runs, there was no indication that a

545   particular LES forcing configuration (75 or 150 km) was consistently preferable. The finding may

546   be loosely attributed to the offsetting nature of several bulk forcing measures discussed above.

547   Specifically, stronger large-scale upward motion was associated with reduced moisture and

548   potential temperature advection contributions. Differences in forcing contributions do not

549   always combine to produce such a serendipitous balance, however. For example, the 1500 UTC

550   simulations exhibited a dramatic spread between the 75 km and 150 km domain variants (e.g.,

551   Tables 2 and 3), with the 1500s_150 run yielding the smallest 6-hour total precipitation (0.61

552   mm), in best agreement with the observations. In comparison, the 1500s_75 run rapidly

553   initiated precipitation and predicted the highest 6-hour total (1.66 mm), but better reflected

554   the areal and cloud field properties of the observations.

555

556

6. Conclusions and Key Findings

SAMEX solutions with forcing more closely matched to observations captured several key aspects of the 25 May 2011 cloud event. Our results were encouraging, given the substantial synoptic variability and the highly idealized modeling framework. Here, we present our initial investigations into the sensitivity of LES solutions to changes in spatial and temporal large-scale domain forcing. Our emphasis was to evaluate whether newer scanning radar technologies for cloud and precipitation properties would benefit our effort to assess the influence of the transient nature of the forcing (i.e., time-varying vs. steady-state) on simulation outcome. A summary of the key findings is as follows.

Our initial findings indicate that measurements obtained from scanning radar such as clout-top height distributions better highlighted the differences across the SAMEX simulations. SAMEX simulations initiated using the time-varying forcing configurations better captured cloud regime transitions for this event. While this result may be expected, a preference toward these time-varying runs may not have been as apparent if evaluated according to simpler bulk metrics of cloud properties (cloud fraction, base, or top). There were promising indications that an improved characterization of cloud field spatial inhomogeneities from multiple scanning radar observations or additional measures of horizontal cell distributions (from additional scanning modes) may help differentiate preferable model configurations. Here, simplified attempts to consider more detailed, multidimensional measures of cloud and precipitation geometry from scanning radar systems (e.g., precipitation onset, precipitation area, cloud-top PDFs) demonstrated several key advantages for the time-varying forcing. For example, the cloud-top

29

579   PDF formulated from the SACR (Fig. 3) and KAZR-ARSCL (Fig. 4) were instructive for highlighting

580   a transition to a bimodal cloud system behavior, helping to identify which LES runs were

581   capable of reproducing these features (Fig. 7). Area-mean model precipitation fields exhibited

582   greater short-term temporal variability relative to the observations but were reasonable when

583   averaged over an appropriate timescale. Some of these discrepancies may be attributed to the

584   demanding nature of attempting to model isolated congestus using idealized LES simulations

585   over a relatively small domain forced with horizontally homogeneous conditions.

586   For this event, the characteristic scale of the analysis domain (75 km, 150 km) did not

587   yield significant differences in the observations, although select simulation results were found

588   sensitive to scale of the forcing (e.g., differences in precipitation for the two 1500 UTC

589   simulations). Linking persistent biases in simulation results to differences in the scale of the

590   forcing or bulk measures of forcing terms (e.g., Table 1) was difficult, however, suggesting that

591   bulk representations of forcing quantities are insufficient in understanding cloud system

592   evolution. Understanding possible secondary linkages was also challenging. For example, total

593   precipitation was unrelated to the LES solutions having the deepest congestus tops or greatest

594   areal precipitation coverage. While we were encouraged by our initial explorations using

595   scanning radar, more complete observations of cloud properties are required (multiple radar

596   views, improved scan modes) to better constrain three-dimensional cloud behavior (e.g., cloud

597   thickness, cloud field topology).

598   Most CRMs or GCMs, including models used in previous studies to represent the

599   transition from shallow cumulus to deeper precipitating clouds, have employed bulk rather

600   than bin microphysical parameterizations (e.g., Grabowski et al. 2006; Kuang and Bretherton

601   2006; Khairoutdinov and Randall 2006; Wu et al. 2009; Hohenegger and Stevens 2013;

602   Mechem and Oberthaler 2013). Our choice of bin microphysics was made in order to eventually

603   foster the most accurate comparisons possible with the ARM spectral radar observations. Our

604   simulation ensemble framework and comparison with a wide range of observational metrics

605   derived from ARM observations will enable future evaluations of different bulk microphysical

606   parameterizations. Performing both bin and bulk LES runs will promote not only comparisons of

607   cloud macroscale properties but also evaluations of the validity of assumptions inherent in the

608   bulk parameterizations (e.g., assumed drop-size distributions or calculations of dispersion in 2-

609   moment parameterizations).

610

633   of this manuscript, or allow others to do so, for United States Government purposes.

634

635

636

637

638 **References**

639

640 Ackerman, T. P., and G. M. Stokes (2003), The Atmospheric Radiation Measurement Program,

641   *Physics Today*, 56(1), 38-44. doi:10.1063/1.1554135.

642

643 Ackerman, A. S., and Coauthors (2009), Large-eddy simulations of a drizzling, stratocumulus-

644   topped marine boundary layer, *Mon. Wea. Rev.*, **137**, 1083–1110.

645

646 Bedacht, E., S. K. Gulev, and A. Macke (2007), Intercomparison of global cloud cover fields over

647   oceans from the VOS observations and NCEP/NCAR reanalysis*, Int. J. Climatol.*, **27**, 1707–

648   1719. doi: 10.1002/joc.1490.

649

650 Bony, S., and J. Dufresne (2005), Marine boundary layer clouds at the heart of tropical cloud

651   feedback uncertainties in climate models, *Geophys. Res. Lett.*, **32**, L20806,

652   doi:10.1029/2005GL023851.

653

654 Borque, P., P. Kollias, and S. Giangrande (2014), First Observations of Tracking Clouds Using

655   Scanning ARM Cloud Radars, *J. Appl. Meteorol. and Climatol*., 53, 2732–2746.

656

657 Bretherton, C. S., and coauthors (1999), An intercomparison of radiatively- driven entrainment

658   and turbulence in a smoke cloud, as simulated by different numerical models, *Quart. J.*

659   *Roy. Meteor. Soc.*, **125**, 391-423.

660

661   Brown, A. R., and Coauthors (2002), Large-eddy simulation of the diurnal cycle of shallow

662   cumulus convection over land*, Quart. J. Roy. Meteor. Soc.*, **128**, 1075–1093.

663

664   Clothiaux, E. E., T. P. Ackerman, G. G. Mace, K. P. Moran, R. T. Marchand, M. A. Miller, and B. E.

665   Martner (2000), Objective determination of cloud heights and radar reflectivities using a

666   combination of active remote sensors at the ARM CART sites, *J. Appl. Meteorol.*, **39**, 645.

667

668   Doviak, R. J., and D. S. Zrnic (1993), Doppler Radar and Weather Observations. Courier Dover

669   Publications, Mineola, NY, 562 pp.

670

671   Faloona, I., D. H. Lenschow, T. Campos, B. Stevens, M. Van Zanten, B. Blomquist, D. Thornton,

672   Alan Bandy, and Hermann Gerber (2005), Observations of entrainment in eastern Pacific

673   marine stratocumulus using three conserved scalars, *J. Atmos. Sci.*, **62**, 3268–3285.

674

675   Giangrande, S. E., E. P. Luke, and P. Kollias (2012), Characterization of Vertical Velocity and Drop

676   Size Distribution Parameters in Widespread Precipitation at ARM Facilities, *J. Appl.*

677   *Meteor. Climatol.*, **51**, 380–391.

678

679   Giangrande, S.E., S. Collis, A. Theisen and A. Tokay (2014), Precipitation Estimation from the

680   ARM Distributed Radar Network During the MC3E Campaign, *J. Appl. Meteor. Climatol.*,

681   53, 2130–2147.

682

683   Grabowski, W. W., P. Bechtold, A. Cheng, R. Forbes, C. Halliwell, M. Khairoutdinov, S. Lang, T.

684   Nasuno, J. Petch, W.-K. Tao, R. Wong, X. Wu, and K.-M. Xu (2006), Daytime convective

685   development over land: A model intercomparison based on LBA observations, *Quarterly*

686   *Journal of the Royal Meteorological Society*, *132*(615), 317-344.

687

688   Hartmann, D. L., M. E. Ockert-Bell, and M. L. Michelsen (1992), The Effect of Cloud Type on

689   Earth's Energy Balance: Global Analysis, *J. Climate*, **5**, 1281–1304.

690

691   Hohenegger, C., and B. Stevens (2013), Preconditioning deep convection with cumulus

692   congestus, *Journal of the Atmospheric Sciences*, *70*(2), 448-464.

693

694   Illingworth, A. J., R. J. Hogan, E. J. O'Connor, D. Bouniol, M. E. Brooks, J. Delanoe, D. P. Donovan,

695   J. D. Eastment, N. Gaussiat, J. W. F. Goddard, M. Haeffelin, H. Klein Baltink, O. A. Krasnov,

696   J. Pelon, J.-M. Piriou, A. Protat, H. W. J. Russchenberg, A. Seifert, A. M. Tompkins, G.-J. van

697   Zadelhoff, F. Vinit, U. Willen, D. R. Wilson, and C. L. Wrench (2007), Cloudnet: Continuous

698   evaluation of cloud profiles in seven operational models using ground-based

699   observations, *Bull. Am. Meteorol. Soc.*, **88**, 883-898.

700

701   Jensen, M.P. and A.D. Del Genio (2006), Factors limiting convective cloud top height at the ARM

702   Nauru Island climate research facility, *J. Climate*, **19**, 2105-2117.

703

704 Jensen, M. P., T. Toto, D. Troyan, P. Ciesielski, D. Holdridge, J. Kyrouac, J. Schatz, Y. Znag and S.

705   Xie (2015), The MC3E Sounding Network: Operations, Processing and Analysis, *Atmos.*

706   *Meas. Tech.*, **8**, 1-14, doi:10.5194/amt-8-1-2015.

707

708 Jensen and Coauthors (2010), Midlatitude Continental Convective Clouds Experiment (MC3E),

709   DOE/SC-ARM/10-0004.

710

711 Johnson, R. H., Rickenbach, T. M., Rutledge, S. A., Ciesielski, P. E., and Schubert, W. H. (1999),

712   Trimodal Characteristics of Tropical Convection, *Journal of Climate*, **12(8),** 2397-2418.

713

714 Kassianov, E., Long, C. N., and Christy, J. (2005), Cloud-base-height estimation from paired

715   ground-based hemispherical observations. *Journal of Applied Meteorology*, **44(8)**, 1221-

716   1233.

717

718 Khairoutdinov, M. F., and D. A. Randall (2003), Cloud resolving modeling of the ARM summer

719   1997 IOP: Model formulation, results, uncertainties, and sensitivities, *J. Atmos. Sci.*, **60**,

720   607–625.

721

722 Khairoutdinov, M., and D. Randall (2006), High-resolution simulation of shallow-to-deep

723   convection transition over land, *Journal of the atmospheric sciences*, *63*(12), 3421-3436.

724

725 Khairoutdinov, M. F., S. K. Krueger, C.- H. Moeng, P. A. Bogenschultz, and D. A. Randall (2009),

726   Large-eddy simulation of marine deep tropical convection, *J. Adv. Model. Earth Syst.*, **1**,

727   15, doi:10.3894/JAMES.2009.1.15.

728

729   Klein, Stephen A., Dennis L. Hartmann (1993), The Seasonal Cycle of Low Stratiform Clouds, *J.*

730   *Climate*, **6**, 1587–1606.

731

732   Kogan, Y. L. (1991), The simulation of a convective cloud in a 3-D model with explicit

733   microphysics. Part I: Model description and sensitivity experiments, *J. Atmos. Sci.*, **48**,

734   1160–1189.

735

736   Kogan, Y. L., D. B. Mechem, and K. Choi (2012), Effects of sea-salt aerosols on precipitation in

737   simulations of shallow cumulus, *J. Atmos. Sci.*, **69**, 463-483.

738

739   Kollias, Pavlos, Bruce A. Albrecht, Eugene E. Clothiaux, Mark A. Miller, Karen L. Johnson, and

740   Kenneth P. Moran (2005), The Atmospheric Radiation Measurement Program Cloud

741   Profiling Radars: An Evaluation of Signal Processing and Sampling Strategies, *J. Atmos.*

742   *Oceanic Technol.*, **22**, 930–948.

743

744   Kollias, P., J. Rémillard, E. Luke, and W. Szyrmer (2011), Cloud radar Doppler spectra in drizzling

745   stratiform clouds: 1. Forward modeling and remote sensing applications, *J. Geophys. Res.*,

746   **116**, D13201.

747

748   Kollias, P., and Coauthors (2014), Scanning ARM Cloud Radars. Part II: Data Quality Control and

749   Processing, *J. Atmos. Oceanic Technol.*, **31**, 583–598.

750

751   Kuang, Z., and C. S. Bretherton, C. S. (2006), A mass-flux scheme view of a high-resolution

752   simulation of a transition from shallow to deep cumulus convection, *Journal of the*

753   *Atmospheric Sciences*, *63*(7), 1895-1909.

754

755   Lasher–Trapp, S. G., C. A. Knight, and J. M. Straka (2001), Early radar echoes from ultragiant

756   aerosol in a cumulus congestus: Modeling and observations, *J. Atmos. Sci.*, **58**, 3545–3562.

757

758   Lenderink, G., and Coauthors (2004), The diurnal cycle of shallow cumulus clouds over land: A

759   single-column model intercomparison study, *Quarterly Journal of the Royal*

760   *Meteorological Society*, **130**, no. 604, 3339-3364.

761

762   Long, C. N., J. M. Sabburg, J. Calbó, and D. Pagès (2006), Retrieving cloud characteristics from

763   ground-based daytime color all-sky images. *Journal of Atmospheric and Oceanic*

764   *Technology*, ***23(5),*** 633-652.

765

766   Luke, E. P., and P. Kollias (2013), Separating Cloud and Drizzle Radar Moments during

767   Precipitation Onset Using Doppler Spectra, *J. Atmos. Oceanic Technol.*, **30**, 1656–1671.

768

769   Luo, Z. J., G. Y. Liu, and G. L. Stephens (2010), Use of A-Train data to estimate convective

770   buoyancy and entrainment rate, *Geophys. Res. Lett.*, **37**, L09804.

771

772 Mace G. G., Q. Zhang, M. Vaughan, R. Marchand, G. Stephens, C. Trepte, and D. Winker (2009),

773   A description of hydrometeor layer occurrence statistics derived from the first year of

774   merged CloudSat and CALIPSO data, *J. Geophys. Res.*, 114 D00A26,

775   doi:10.1029/2007JD009755.

776

777 Mather, J. H., and J. W. Voyles (2013), The Arm Climate Research Facility: A Review of Structure

778   and Capabilities, *Bull. Amer. Meteor. Soc.,* **94**, 377–392.

779

780 Mechem, D. B., Y. L. Kogan, and D. M. Schultz (2010), Large-eddy simulation of post-cold-frontal

781   continental stratocumulus, *J. Atmos. Sci.*, **67**, 3835-3853.

782

783 Mechem, D. B., S. E. Yuter, and S. P. de Szoeke (2012), Thermodynamic and aerosol controls in

784   southeast Pacific stratocumulus, *J. Atmos. Sci.*, **69,** 1250-1266.

785

786 Mechem, D. B., and A. J. Oberthaler (2013), Numerical simulation of tropical cumulus congestus

787   during TOGA COARE, *J. Adv. Model. Earth Syst.*, **5**, 1-15, doi:10.1002/jame.20043.

788

789 Medeiros, B., B. Stevens, I. M. Held, M. Zhao, D. L. Williamson, J. G. Olson, and C. S. Bretherton

790   (2008), Aquaplanets, climate sensitivity, and low clouds, *J. Climate*, **21**, 4974–4991.

791

792   Mesinger, F., G. DiMego, E. Kalnay, K. Mitchell, P. C. Shafran, W. Ebisuzaki, D. Jovic, J. Woollen,

793   E. Rogers, E. H. Berbery, *et al*. (2006), North American regional reanalysis. *Bull. Am.*

794   *Meteorol. Soc.*, **87**, 343–360.

795

796   Minnis, P., S. Sun-Mack, D. F. Young, P. W. Heck, D. P. Garber, Y. Chen, D. A. Spangenberg, R. F.

797   Arduini, Q. Z. Trepte, W. L. Smith, Jr., J. K. Ayers, S. C. Gibson, W. F. Miller, V. Chakrapani,

798   Y. Takano, K.-N. Liou, Y. Xie, and P. Yang (2011), CERES Edition-2 cloud property retrievals

799   using TRMM VIRS and Terra and Aqua MODIS data, Part I: Algorithms, *IEEE Trans. Geosci.*

800   *Remote Sens.*, **49**, 11, 4374-4400.

801

802   Moeng, C.-H., and Coauthors (1996), Simulation of a stratocumulus-topped PBL:

803   Intercomparison among different numerical codes, *Bull. Amer. Meteor. Soc.*, **77**, 261–278.

804

805   Morrison, H., J. A. Curry, and V. I. Khvorostyanov, 2005: A new double-moment microphysics

806   parameterization for application in cloud and climate models. Part I: Description. *J. Atmos.*

807   *Sci.*, **62**, 1665–1677.

808

809   Rauber, R., and Coauthors (2007), Rain in (shallow) cumulus over the ocean: The RICO

810   campaign, *Bull. Am. Meteorol. Soc.*, **88**, 1912–1928.

811

812   Riehl, H., C. Yeh, J. S. Malkus, and N. E. LaSeur (1951), The north-east trade of the Pacific Ocean,

813   *Quart. J. Roy. Meteor. Soc.,* **77,** 598–626.

814

815   Ryzhkov, A. V., S. E. Giangrande, V. M. Melnikov, and T. J. Schuur (2005), Calibration Issues

816   of Dual-Polarization Radar Measurements, *J. Atmos. Oceanic Technol.*, **22**, 1138–1155.

817

818   Siebesma, A. P., and Coauthors (2003), A large-eddy simulation study of shallow cumulus

819   convection, *J. Atmos. Sci.*, **60,** 1201–1219.

820

821   Stevens, B., and Coauthors (2001), Simulations of trade wind cumuli under a strong inversion*, J.*

822   *Atmos. Sci.*, **58**, 1870–1891.

823

824   Stevens, B., and Coauthors (2003), Dynamics and chemistry of marine stratocumulus —

825   DYCOMS-II, *Bull. Amer. Meteor. Soc.*, **84**, 579–593.

826

827   Stevens, B., and Coauthors (2005), Evaluation of large-eddy simulations via observations of

828   nocturnal marine stratocumulus, *Mon. Wea. Rev.,* **133**, 1443–1462.

829

830   Stevens, B. (2007), On the growth of layers of nonprecipitating cumulus convection, *J. Atmos.*

831   *Sci.,* **64,** 2916–2931.

832

833   Stevens, B., and S. Bony (2013), What are climate models missing?, *Science*, **340**(6136), 1053–

834   1054, doi:10.1126/science.1237554.

835

836   Stokes, G. M., & Schwartz, S. E. (1994), The Atmospheric Radiation Measurement (ARM)

837   Program: Programmatic background and design of the cloud and radiation test bed,

838   *Bulletin of the American Meteorological Society*, **75(7)**, 1201-1221.

839

840   van Zanten, M. C., B. Stevens, L. Nuijens, A. P. Siebesma, A. Ackerman, F. Burnet, A. Cheng, F.

841   Couvreaux, H. Jiang, M. Khairoutdinov, Y. Kogan, D. C. Lewellen, D. Mechem, K. Nakamura,

842   A. Noda, B. Shipway, J. Slawinska, S. Wang, and A. Wyszogrodzki (2011), Controls on

843   precipitation and cloudiness in simulations of trade-wind cumulus as observed during

844   RICO, *J. Adv. Model. Earth Syst.*, **3**, M06001, doi:10.3894/JAMES.2011.3.5.

845

846   Vogelmann, Andrew M., and Coauthors (2012), Racoro Extended-Term Aircraft Observations of

847   Boundary Layer Clouds, *Bull. Amer. Meteor. Soc.*, **93**, 861–878.

848

849   Waite, M. L., and B. Khouider (2010), Deepening of tropical convection by congestus

850   preconditioning, *J. Atmos. Sci.*, **67**, 2601–2615.

851

852   Walsh, J. E., W. L. Chapman, and D. H. Portis (2009), Arctic Cloud Fraction and Radiative Fluxes

853   in Atmospheric Reanalyses, *J. Climate*, **22**, 2316–2334.

854

855   Wilkinson, J. M., R. J. Hogan, A. J. Illingworth, and A. Benedetti (2008), Use of a lidar forward

856   model for global comparisons of cloud fraction between the ICESat lidar and the ECMWF

857   model, *Mon. Weather Rev*., **136**, 3742 – 3759.

858

859   Wiscombe, W. J. (2005), Scales, tools and reminiscences. In *3D Radiative Transfer in Cloudy*

860   *Atmospheres* (pp. 3-92). Springer Berlin Heidelberg.

861

862   Wu, C. M., B. Stevens, and A. Arakawa (2009), What controls the transition from shallow to

863   deep convection?, *Journal of the Atmospheric Sciences*, *66*(6), 1793-1806.

864

865   Wu, X., W. W. Grabowski, and M. W. Moncrieff (1998), Long-term behavior of cloud systems in

866   TOGA COARE and their interactions with radiative and surface processes. Part I: Two-

867   dimensional modeling study, *J. Atmos. Sci.*, **55**, 2693–2714.

868

869   Wu, W., Y. Liu, M. P. Jensen, T. Toto, M. J. Foster, and C. N. Long (2014), A comparison of

870   multiscale variations of decade-long cloud fractions from six different platforms over the

871   Southern Great Plains in the United States, *J. Geophys. Res. Atmos.*, **119**,

872   doi:10.1002/2013JD019813.

873

874   Wyant, M. C., and Coauthors (2007), A single-column model intercomparison of a heavily

875   drizzling stratocumulus-topped boundary layer, *J. Geophys. Res.*, **112**, D24204.

876

877   Xie, S., and Coauthors (2005), Simulations of midlatitude frontal clouds by single-column and

878   cloud-resolving models during the Atmospheric Radiation Measurement March 2000

879   cloud intensive operational period, *J. Geophys. Res.,* **110**, D15S03.

880

881   Xie, S., Y. Zhang, S.E. Giangrande, M.P. Jensen, R. McCoy and M. Zhang (2014), Interactions

882   between Cumulus Convection and Its Environment Revealed by MC3E Sounding Array, *J.*

883   *Geophys. Res.*, submitted.

884

885   Xie, Y., and Y. Liu (2013), A new approach for simultaneously retrieving cloud albedo and cloud

886   fraction from surface-based shortwave radiation measurements, *Environ. Res. Lett.*, **8**,

887   044023.

888

889   Xu, K-M., and Coauthors (2002), An intercomparison of cloud-resolving models with the

890   Atmospheric Radiation Measurement summer 1997 Intensive Observation Period data,

891   *Quart. J. Roy. Meteor. Soc.,* **128,** 593–624.

892

893   Xu, K.-M., and Coauthors (2005), Modeling springtime shallow frontal clouds with cloud-

894   resolving and single-column models, *J. Geophys. Res.*, **110**, D15S04.

895

896   Young, B. C., A. A. Bradley, W. F. Krajewski, A. Kruger, and M. L. Morrissey (2000), Evaluating

897   NEXRAD Multisensor Precipitation Estimates for Operational Hydrologic Forecasting, *J.*

898   *Hydrometeor*, **1**, 241–254.

899

900   Zeng, X., W.-K. Tao, M. Zhang, A. Y. Hou, S. Xie, S. Lang, X. Li, D. C. O'Starr, X. Li, and J. Simpson

901   (2009), An indirect effect of ice nuclei on atmospheric radiation, *J. Atmos. Sci.*, **66**, 41–61.

902

903   Zhang, M. H., and J. L. Lin (1997), Constrained variational analysis of sounding data bases on

904   column-integrated budgets of mass, heat, moisture, and momentum: Approach and

905   application to ARM measurements, *J. Atmos. Sci.,* **54**, 1503-1524.

906

907   Zhang, J., K. Howard, and J. J. Gourley (2005), Constructing Three-Dimensional Multiple-Radar

908   Reflectivity Mosaics: Examples of Convective Storms and Stratiform Rain Echoes, *J. Atmos.*

909   *Oceanic Technol.*, **22**, 30–42.

910

911   Zhu, P, and Coauthors (2005), Intercomparison and interpretation of single-column model

912   simulations of a nocturnal stratocumulus-topped marine boundary layer, Mon. Wea. Rev.,

913   **133**, 2741–2758.

914

915

916   **Figure Captions**

917

918   Figure 1. Synoptic configuration at 1800 UTC. Albedo from GOES visible satellite imagery is

919   combined with isobars of the surface pressure field [in hPa] from North American Regional

920   Reanalysis (NARR; Mesinger et al. 2006) and a multi-radar composite of reflectivity from WSR–

921   88D NEXRAD radars. The magenta "X" represents the location of the ARM Central Facility, and

922   the multiple "S"s indicate MC3E sounding sites. Concentric circles represent the analysis

923   volumes of the 75-km and 150-km variation analysis domains.

924

925   Figure 2. Time-height sections of potential temperature and moisture advection, large-scale

926   vertical velocity, and surface sensible and latent heat fluxes at two different analysis scales. The

927   SAMEX forcing for the different simulations is constructed from different combinations of

928   vertical profiles, denoted by the red vertical lines inside the rose boxes. The rose shading

929   denotes the time period for which simulations are performed.

930

931   Figure 3. (a) Histogram of cloud-top heights from the SACR as a function of time. (b) Rain rate

932   from the disdrometer at the SGP central facility and an averaged radar-derived estimate from

933   the C-SAPR using a standard Oklahoma Z–R relationship along the SACR scanning path. Shaded

934   regions indicate the presence of precipitation as recorded by the disdrometer, and arrows in (b)

935   indicate periods of heavier area-mean precipitation measured by the C-SAPR. Adapted from

936   Borque et al. (2014).

937

938   Figure 4. (a) Frequency of occurrence of highest cloud top under 6 km, calculated from KAZR–

939   ARSCL cloud top product and binned in intervals of 20 minutes in time and 250 m in the

940   vertical. (b) Time-height section derived from KAZR–ARSCL of hydrometeor fraction, averaged

941   over 20-minute intervals, overlaid with cloud top (black dots).

942

943   Fig. 5. Snapshot of the simulated reflectivity field from the 1200v_75 control simulation,

944   calculated directly from the bin-microphysics drop size distributions. (a) Plan view of column-

945   maximum reflectivity. Solid black contours are 0 dBz, representative of typical C-band radar

946   sensitivity. (b) and (c) represent vertical cross sections taken through the northern and

947   southern regions of the domain in (a).

948

949   Figure 6. A series of imagery from the TSI (top). Five observational estimates of cloud fraction,

950   all denoted by blue lines overlaid on cloud fraction calculated from the simulation suite

951   (bottom). The black line represents the control (1200v_75) simulation. The dashed gray line is

952   the ensemble median, and the gray bands represent the minimum and maximum cloud fraction

953   values of the simulation ensemble. The rose shaded area indicates the period covered by the

954   TSI images.

955

956   Figure 7. Time-varying PDFs of cloud-top height for six of the simulations. The white line

957   represents the time of precipitation onset, taken to be a precipitation rate of 1 mm d^{-1} at the

958   surface.

959

960 Figure 8. (a) Time series of echo area fraction from the C-SAPR and the simulation ensemble.

961 The width of the bands two C-SAPR time series represents precipitation area defined by area

962 bound by 30 and 25 dBz values. The dashed gray line is the ensemble median, and the gray

963 bands represent the ensemble minimum and maximum, corresponding to a 30 dBz reflectivity

964 threshold. The black line represents the echo area fraction of the control (1200v_75)

965 simulation. (b) Accumulated precipitation from the model ensemble (black, dashed gray, and

966 gray envelope), along with observational estimates at two scales from the NEXRAD NMQ.

967

968

969

970

971   **Table Captions**

972

973   Table 1. Description of simulation suite. The mean forcing terms for the two time-varying

974   simulations represent density-weighted mean values from the surface to 640 mb over the early

975   (3–6 h) and late periods (6–9 h) of the simulations.

976

977   Table 2. Summary of simulation results from the early period of the simulation (3–6 h). Data

978   columns represent mean cloud fraction (median in parentheses); median cloud-top height

979   (90th percentile height in parentheses); precipitation onset time (defined as the time when the

980   surface precipitation rate first reaches the threshold value of 1 mm d^{-1}); range of mean and

981   median precipitation area fraction (area fraction of 30 and 25 dBz echo); and total precipitation

982   accumulated over the 3-h period.

983

984   Table 3. Summary of simulation results from the late period of the simulation (6–9 h). Column

985   quantities are defined as in Table 2.
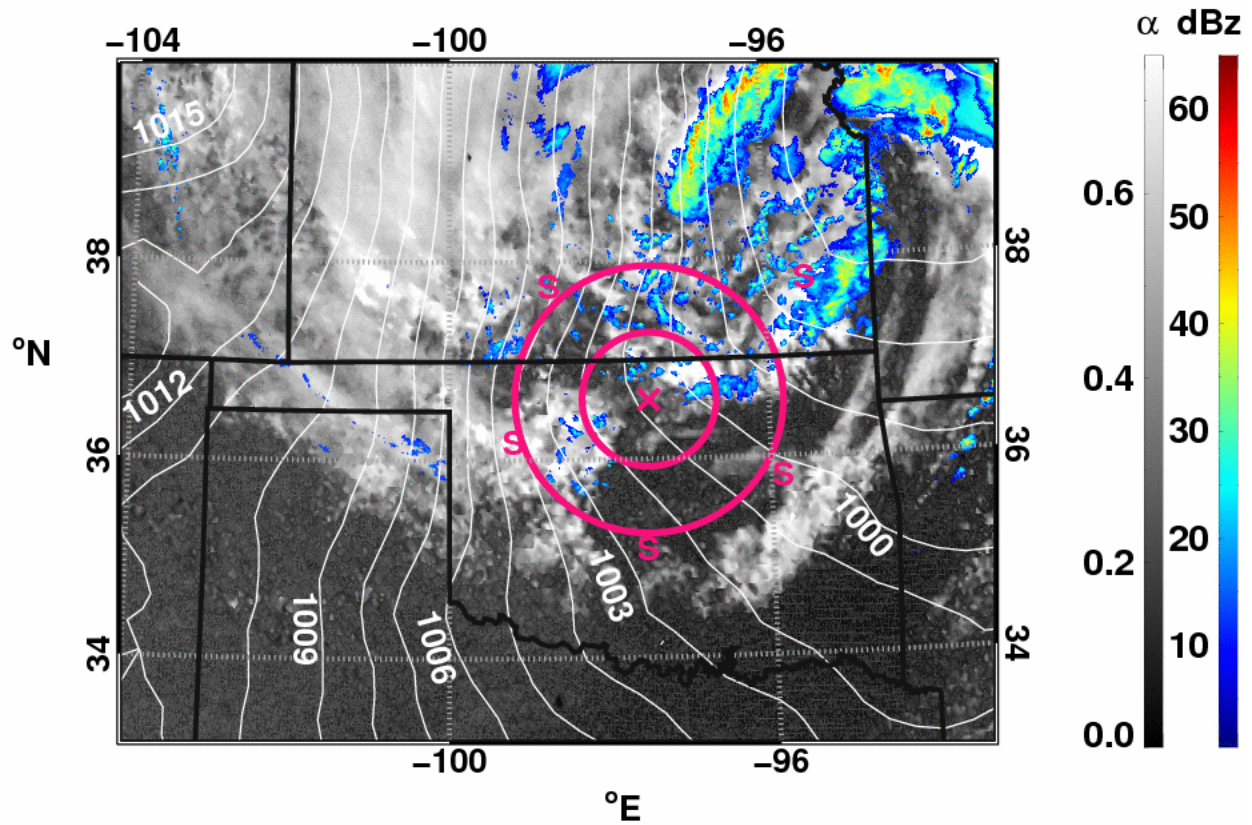
986

987

988

989

990

991

992   Figure 1. Synoptic configuration at 1800 UTC. Albedo from GOES visible satellite imagery is

993   combined with isobars of the surface pressure field [in hPa] from North American Regional

994   Reanalysis (NARR; Mesinger et al. 2006) and a multi-radar composite of reflectivity from WSR–

995   88D NEXRAD radars. The magenta "X" represents the location of the ARM Central Facility, and

996   the multiple "S"s indicate MC3E sounding sites. Concentric circles represent the analysis

997   volumes of the 75-km and 150-km variation analysis domains.

998

999

1000

1001
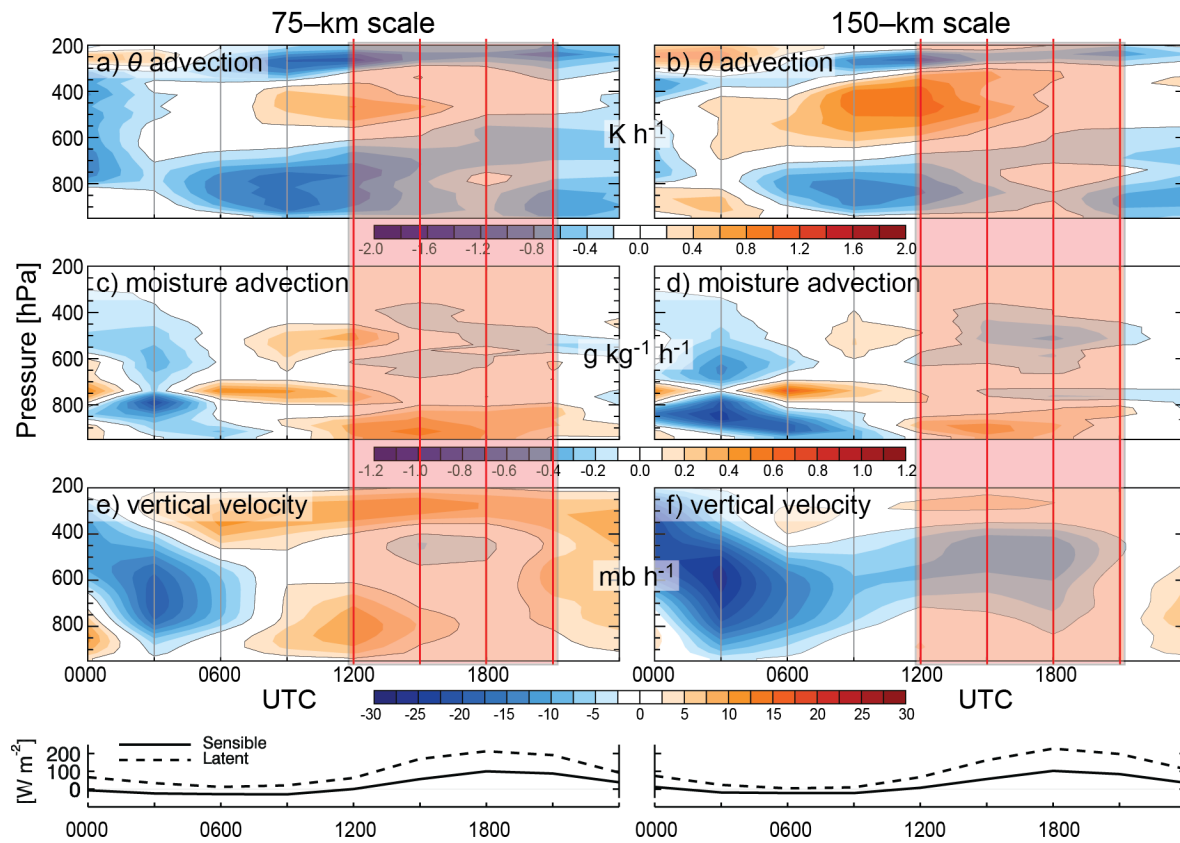
Figure 2. Time-height sections of potential temperature and moisture advection, large-scale vertical velocity, and surface sensible and latent heat fluxes at two different analysis scales. The SAMEX forcing for the different simulations is constructed from different combinations of vertical profiles, denoted by the red vertical lines inside the rose boxes. The rose shading denotes the time period for which simulations are performed.
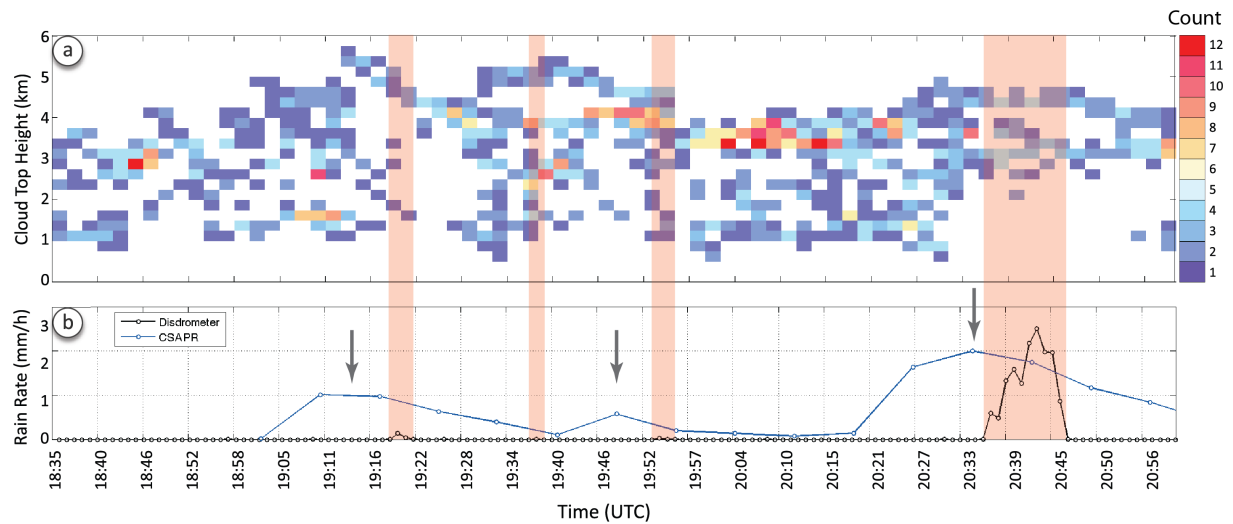
1014

1015

1016

1017

Figure 3. (a) Histogram of cloud-top heights from the SACR as a function of time. (b) Rain rate

from the disdrometer at the SGP central facility and an averaged radar-derived estimate from

the C-SAPR using a standard Oklahoma Z–R relationship along the SACR scanning path. Shaded

regions indicate the presence of precipitation as recorded by the disdrometer, and arrows in (b)

indicate periods of heavier area-mean precipitation measured by the C-SAPR. Adapted from

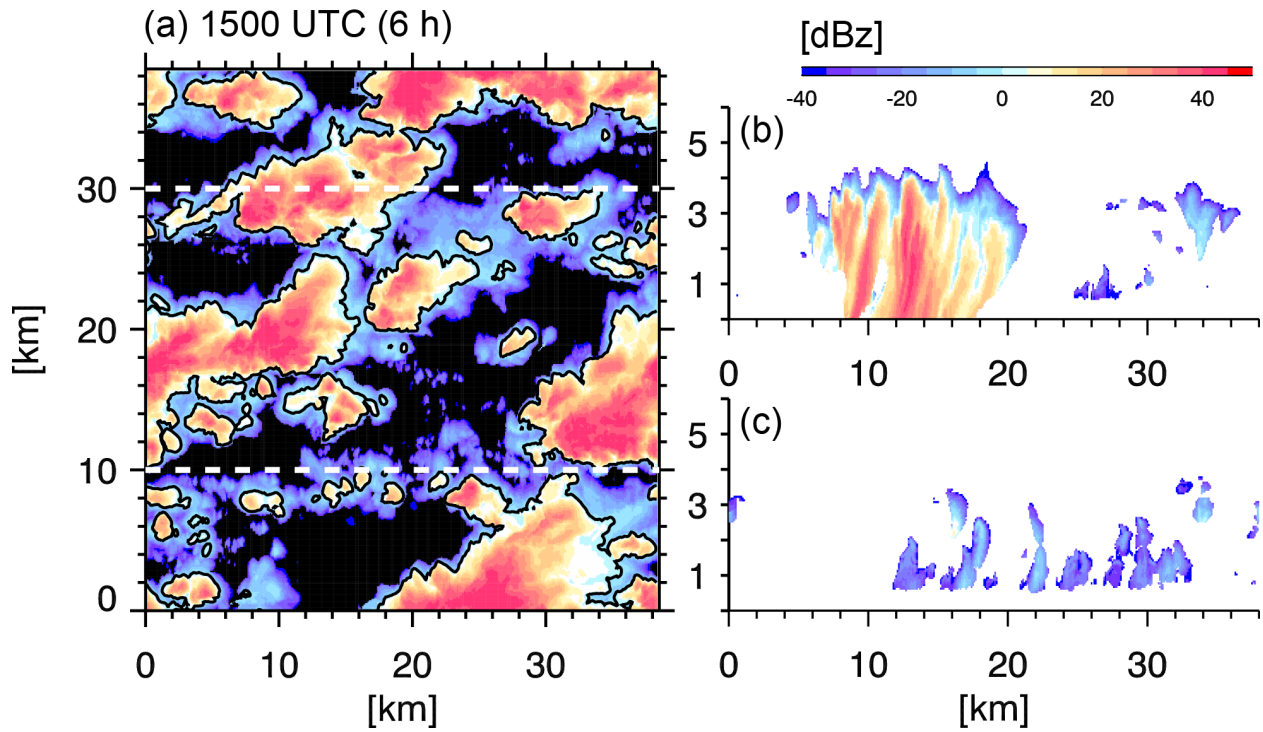Borque et al. (2014).

1024

1025

1026

1027
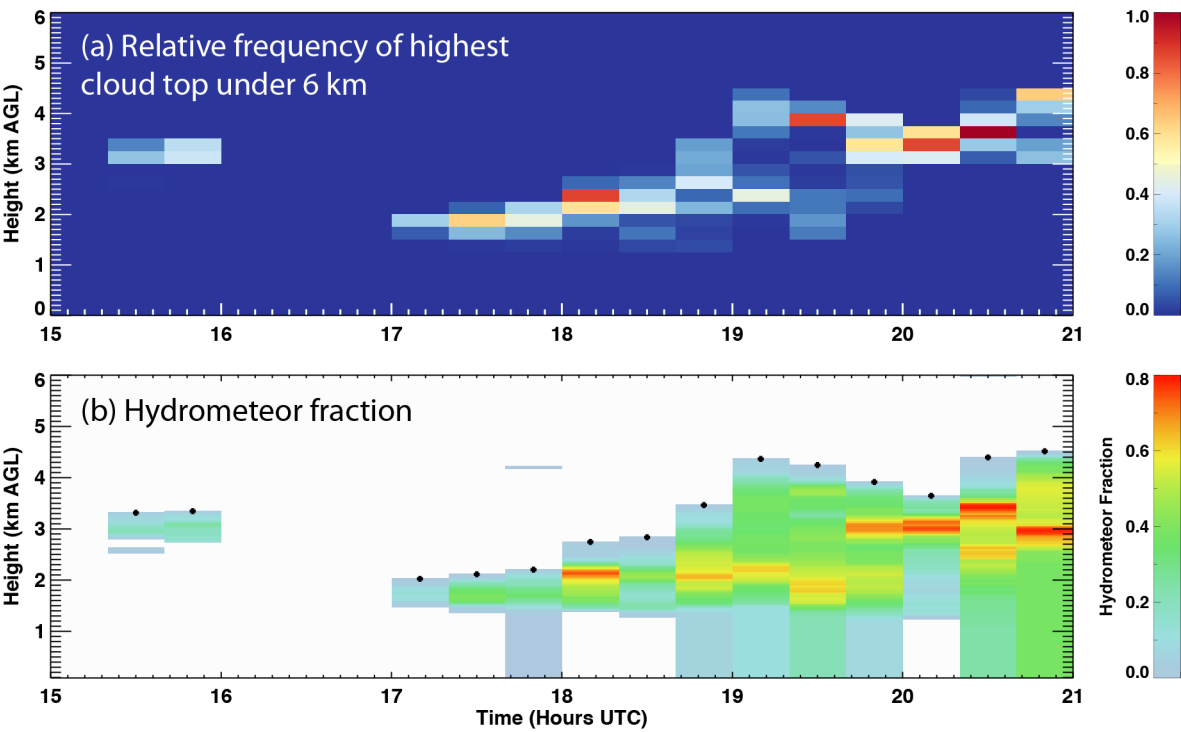
1028

1029 Figure 4. (a) Frequency of occurrence of highest cloud top under 6 km, calculated from KAZR–

1030 ARSCL cloud top product and binned in intervals of 20 minutes in time and 250 m in the

1031 vertical. (b) Time-height section derived from KAZR–ARSCL of hydrometeor fraction, averaged

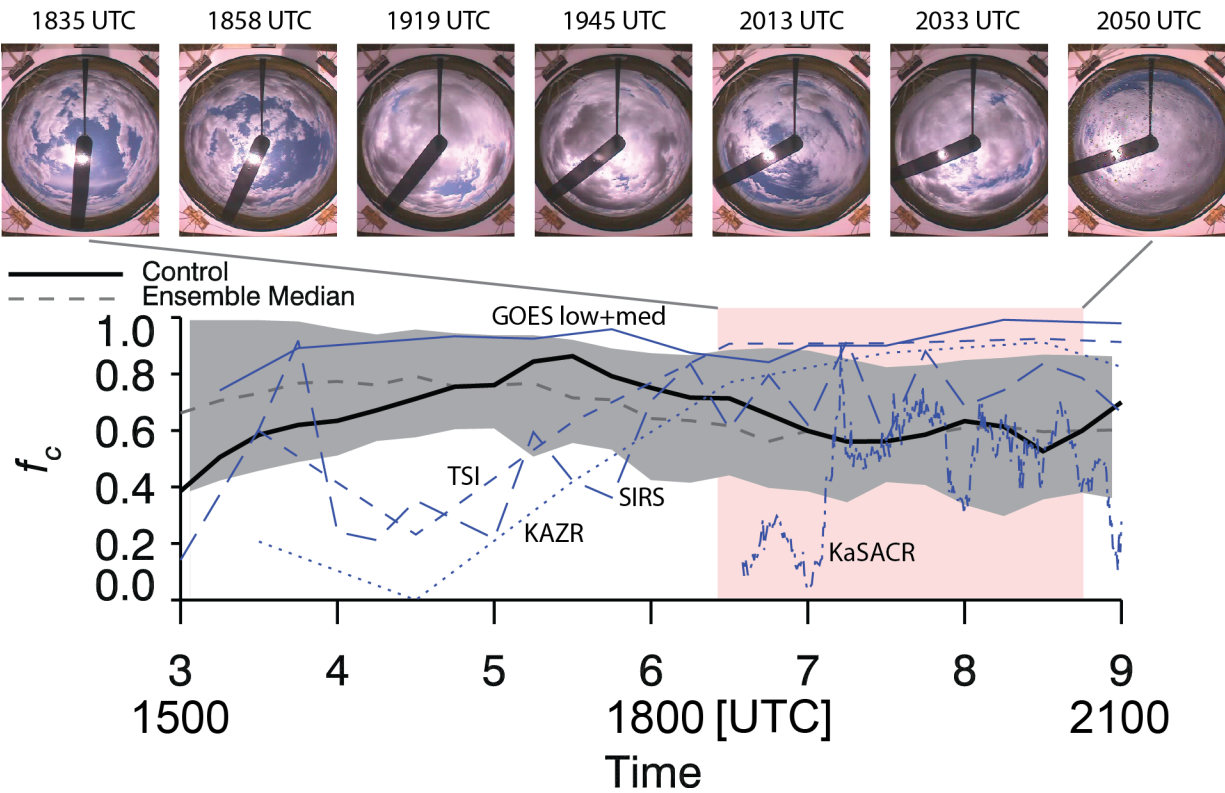1032 over 20-minute intervals, overlaid with cloud top (black dots).

1033

1034

Fig. 5. Snapshot of the simulated reflectivity field from the 1200v_75 control simulation, calculated directly from the bin-microphysics drop size distributions. (a) Plan view of column-maximum reflectivity. Solid black contours are 0 dBz, representative of typical C-band radar sensitivity. (b) and (c) represent vertical cross sections taken through the northern and southern regions of the domain in (a).
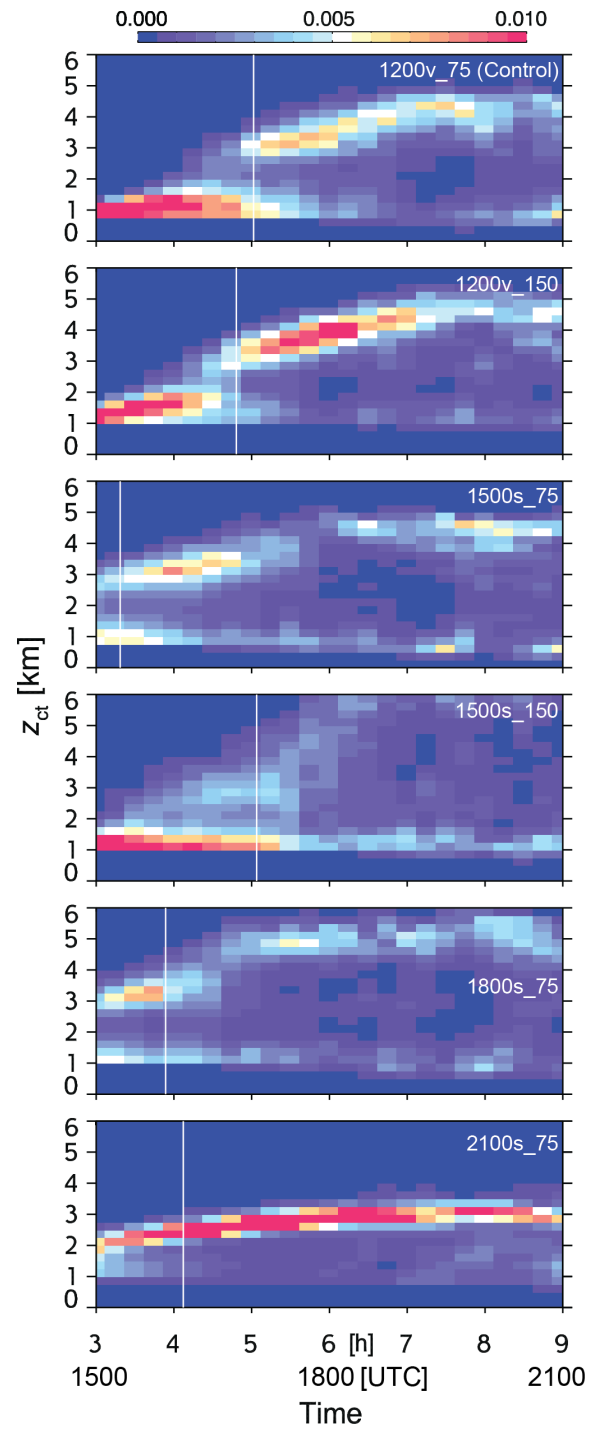
1044

1045

1046

1047 Figure 6. A series of imagery from the TSI (top). Five observational estimates of cloud fraction,

1048 all denoted by blue lines overlaid on cloud fraction calculated from the simulation suite

1049 (bottom). The black line represents the control (1200v_75) simulation. The dashed gray line is

1050 the ensemble median, and the gray bands represent the minimum and maximum cloud fraction

1051 values of the simulation ensemble. The rose shaded area indicates the period covered by the

1052 TSI images.

1053

1054

1055

1056

1057

Figure 7. Time-varying PDFs of cloud-top height for six of the simulations. The white line represents the time of precipitation onset, taken to be a precipitation rate of 1 mm d^{-1} at the surface.
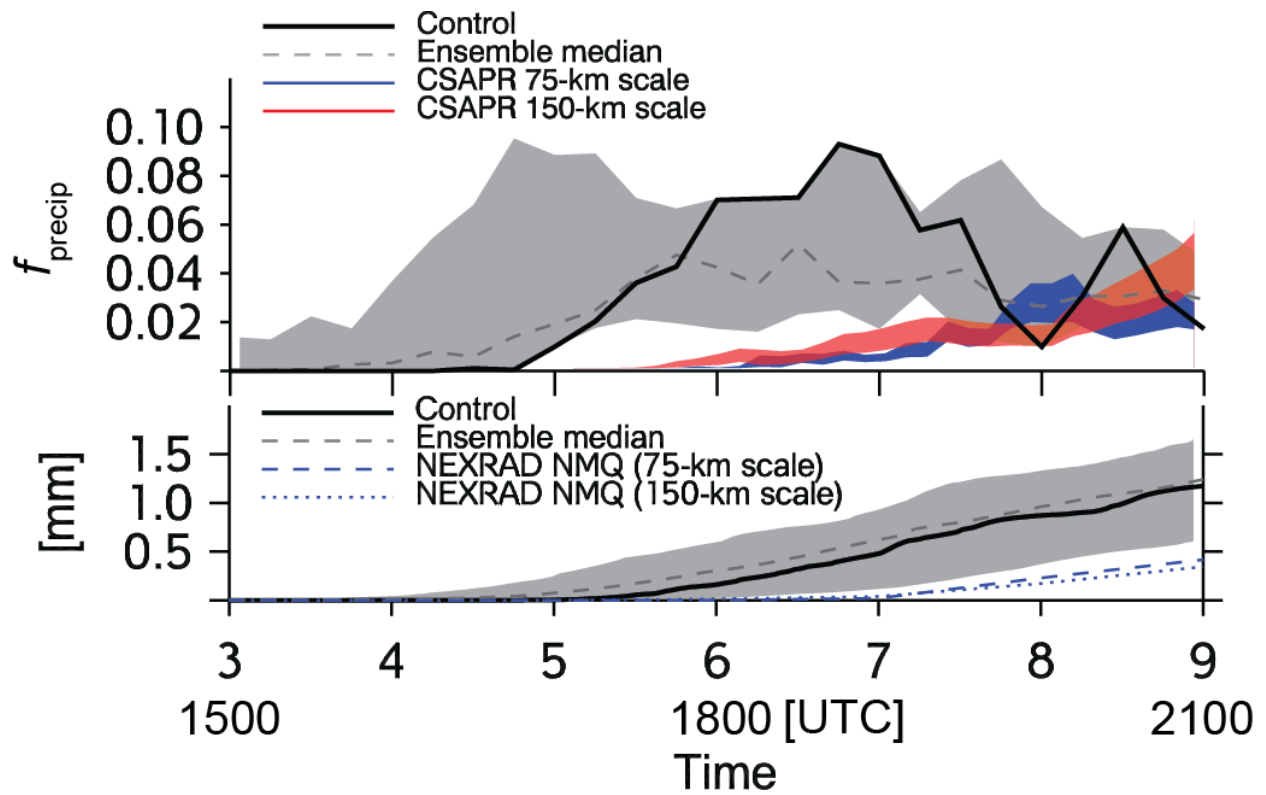
1066 Figure 8. (a) Time series of echo area fraction from the C-SAPR and the simulation ensemble.

1067 The width of the bands two C-SAPR time series represents precipitation area defined by area

1068 bound by 30 and 25 dBz values. The dashed gray line is the ensemble median, and the gray

1069 bands represent the ensemble minimum and maximum, corresponding to a 30 dBz reflectivity

1070 threshold. The black line represents the echo area fraction of the control (1200v_75)

1071 simulation. (b) Accumulated precipitation from the model ensemble (black, dashed gray, and

1072 gray envelope), along with observational estimates at two scales from the NEXRAD NMQ.

1073

1074

1075

1076

1077 Table 1. Description of simulation suite. The mean forcing terms for the two time-varying

1078 simulations represent density-weighted mean values from the surface to 640 mb over the early

1079 (3–6 h) and late periods (6–9 h) of the simulations.

1080

Simulation name	Forcing scale [km]	Time- [v]arying/ [s]teady state	Time or interval of forcing [UTC]	Potential temperature advection [K h^{-1}]		Moisture advection [g kg^{-1} h^{-1}]		Vertical motion [mb h^{-1}]	
1200v_75	75	v	1200–2100	-0.40	-0.30	0.17	0.13	1.33	1.31
1200v_150	150	v	1200–2100	-0.17	-0.25	0.10	0.02	-1.68	-0.01
1500s_75	75	s	1500	-0.47		0.19		2.15	
1500s_150	150	s	1500	-0.24		0.13		-0.96	
1800s_75	75	s	1800	-0.32		0.15		0.52	
1800s_150	150	s	1800	-0.10		0.07		-2.40	
2100s_75	75	s	2100	-0.27		0.10		2.10	

1081
1082
1083
1084
1085
1086

1087   Table 2. Summary of simulation results from the early period of the simulation (3–6 h). Data

1088   columns represent mean cloud fraction (median in parentheses); median cloud-top height

1089   (90th percentile height in parentheses); precipitation onset time (defined as the time when the

1090   surface precipitation rate first reaches the threshold value of 1 mm d^{-1}); range of mean and

1091   median precipitation area fraction (area fraction of 30 and 25 dBz echo); and total precipitation

1092   accumulated over the 3-h period.

1093

Simulation name	CF	CT height [km]	Precip. onset time [h]	Precip. area fraction	Precip. [mm]
1200v_75 (Control)	0.68 (0.71)	1.80 (2.57)	5.0	0.014–0.021 (< 0.01)	0.16
1200v_150	0.74 (0.79)	2.40 (3.04)	4.8	0.014–0.024 (< 0.01)	0.28
1500s_75	0.65 (0.66)	2.85 (3.92)	3.3	0.044–0.060 (0.043–0.060)	0.59
1500s_150	0.54 (0.56)	2.16 (3.64)	5.1	0.019–0.026 (< 0.01)	0.10
1800s_75	0.73 (0.71)	3.57 (4.56)	3.9	0.047–0.064 (0.053–0.077)	0.52
1800s_150	0.87 (0.93)	3.89 (4.92)	4.0	0.050–0.066 (0.063–0.080)	0.57
2100s_75	0.91 (0.93)	2.47 (2.79)	4.1	0.010–0.020 (0.008–0.016)	0.33

1094

1095

1096

1097   Table 3. Summary of simulation results from the late period of the simulation (6–9 h). Column

1098   quantities are defined as in Table 2.

Simulation name	CF	CT height [km]	Precip. onset time [h]	Precip. area fraction	Precip. [mm]
1200v_75 (Control)	0.63 (0.61)	3.56 (4.49)	5.0	0.053–0.074 (0.059–0.078)	1.01
1200v_150	0.72 (0.71)	4.10 (4.88)	4.8	0.048–0.067 (0.047–0.059)	0.97
1500s_75	0.51 (0.55)	3.64 (4.73)	3.3	0.038–0.049 (0.032–0.043)	1.07
1500s_150	0.41 (0.38)	3.07 (6.10)	5.1	0.045–0.056 (0.045–0.051)	0.51
1800s_75	0.60 (0.60)	4.39 (5.48)	3.9	0.050–0.066 (0.053–0.069)	0.76
1800s_150	0.51 (0.48)	3.98 (5.91)	4.0	0.057–0.071 (0.058–0.074)	0.89
2100s_75	0.86 (0.87)	2.88 (3.29)	4.1	0.024–0.041 (0.024–0.039)	0.90

1099

1100

1101

1102